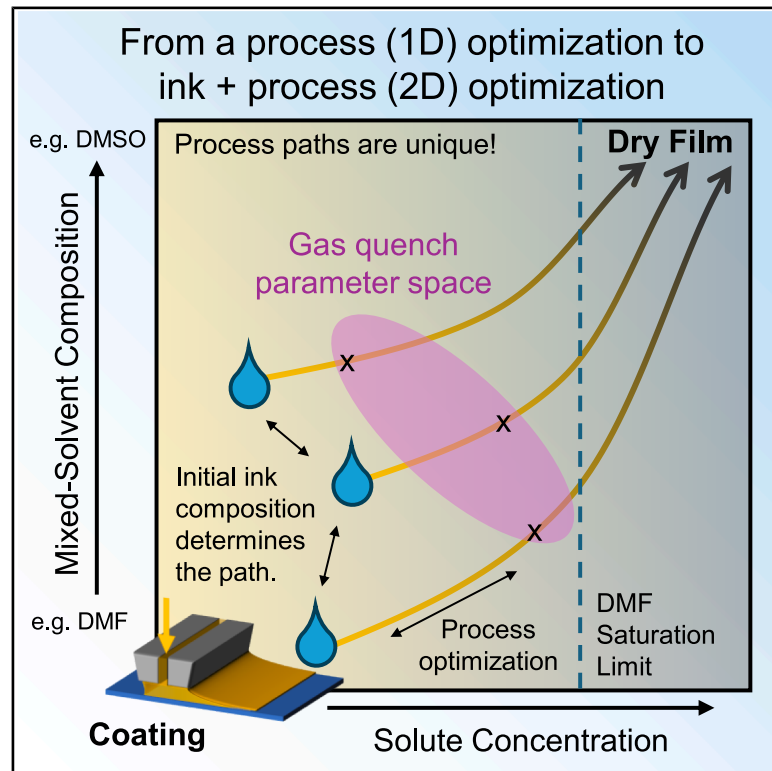


# Formation trajectories of solution-processed perovskite thin films from mixed solvents

## Graphical abstract



## Authors

Jesse L. Starger, Amy E. Louks, Kelly Schutt, ..., Nicolas J. Alvarez, Richard A. Cairncross, Axel F. Palmstrom

## Correspondence

alvarez@drexel.edu (N.J.A.), axel.palmstrom@nrel.gov (A.F.P.)

## In brief

Starger et al. model the dynamic evolution of perovskite ink thin films based on the localized drying environment to capture processing design space. These process maps provide a framework that aims to improve batch-to-batch reproducibility and process transferability and to streamline process development for scalable metal halide perovskite solar cells.

## Highlights

- *In situ* thickness measurements quantify the convective environment during coating
- Process maps aid in the selection of process conditions and formulations
- Process sensitivity estimated by modeling environmental effects on evaporation rate
- Process-path methodology applied to scalable mixed-solvent perovskites



## Article

# Formation trajectories of solution-processed perovskite thin films from mixed solvents

Jesse L. Starger,<sup>1</sup> Amy E. Louks,<sup>2,3</sup> Kelly Schutt,<sup>3</sup> E. Ashley Gaulding,<sup>3</sup> Robert W. Epps,<sup>3</sup> Rosemary C. Bramante,<sup>3</sup> Ross A. Kerner,<sup>3</sup> Kai Zhu,<sup>3</sup> Joseph J. Berry,<sup>3,4,5</sup> Nicolas J. Alvarez,<sup>1,\*</sup> Richard A. Cairncross,<sup>1</sup> and Axel F. Palmstrom<sup>3,6,\*</sup>

<sup>1</sup>Department of Chemical and Biological Engineering, Drexel University, Philadelphia, PA 19104, USA

<sup>2</sup>Department of Chemistry, Colorado School of Mines, Golden, CO 80309, USA

<sup>3</sup>National Renewable Energy Laboratory, Golden, CO 80401, USA

<sup>4</sup>Department of Physics, University of Colorado Boulder, Boulder, CO 80309, USA

<sup>5</sup>Renewable and Sustainable Energy Institute, University of Colorado Boulder, Boulder, CO 80309, USA

<sup>6</sup>Lead contact

\*Correspondence: [alvarez@drexel.edu](mailto:alvarez@drexel.edu) (N.J.A.), [axel.palmstrom@nrel.gov](mailto:axel.palmstrom@nrel.gov) (A.F.P.)

<https://doi.org/10.1016/j.xcrp.2025.102655>

## SUMMARY

The engineering of mixed-solvent formulations and their evaporation conditions are key to reproducible perovskite coatings for high-performance photovoltaics. Here, we report a lumped-parameter evaporation model to predict the evolution of a perovskite ink liquid film over time (solvent ratio, solute concentration, and film thickness). The drying-rate model is validated via *in situ* film-thickness measurements, and the predicted transient liquid film state is mapped as a process path. These methods allow for the prediction of process sensitivity to local environmental factors and the understanding and visualization of a broader processing parameter space enabled through the coupling of process and ink engineering. Process maps are applied to create a new framework for scalable perovskite coating development with a goal of improving the reproducibility and transferability of perovskite fabrication. This approach is demonstrated with blade-coated  $\text{FA}_{0.83}\text{Cs}_{0.17}\text{PbI}_3$  photovoltaic devices, improving the photovoltaic conversion efficiency from  $17.5\% \pm 1.7\%$  to  $20.3\% \pm 0.6\%$ .

## INTRODUCTION

While solution-processed metal halide perovskites (MHPs) offer the potential for thin-film photovoltaics at low cost, the performance of scalable processes and modules have consistently lagged behind those of spin-coated devices.<sup>1,2</sup> At the lab scale, identifying the correct process parameters and associated process paths is often a labor-intensive Edisonian effort that must be re-optimized when scaling up or transferring to a new processing environment. A process path refers to a specific evolution of compositional states a liquid film undergoes during drying. Achieving a dense, compact thin film is essential for realizing high-performance solar cells and modules. Thus, to ensure production of high-quality MHP films, experienced researchers are known to intuitively adjust the formulations “on-the-fly” in response to changing environmental variables such as ambient temperatures, solvent vapor levels, or humidity.

To develop more robust and reproducible processes, two techniques have emerged as standard practice in the field: (1) using mixed-solvent ink formulations and (2) implementing a rapid-evaporation “quench” step.<sup>3</sup> Mixed-solvent systems, such as the combination of *N,N*-dimethylformamide (DMF) with dimethyl sulfoxide (DMSO), are thought to be effective for

widening the process window because the more volatile solvent (DMF) helps control the evaporation dynamics, while the more strongly coordinating solvent (DMSO) directs the crystallization pathway for optimal film formation.<sup>4–9</sup> The “quench” step refers to techniques that accelerate the removal of solvent, such as by exposing the wet film to an anti-solvent,<sup>10</sup> vacuum,<sup>11</sup> heat,<sup>12</sup> or additional convection (e.g., air knife or nitrogen gun).<sup>13,14</sup> A hold period of slow drying prior to the quench is also thought to stabilize a precipitating amorphous “sol-gel” state before crystallization has begun, impacting final solid-film microstructure and device efficiency.<sup>15–17</sup> However, it remains challenging to quantitatively track how the precise composition of the film (solvent ratios and concentration) changes during the solvent removal and film formation process. Developing a quantitative understanding of how film composition evolves during drying is critical for the field to develop a first-principles approach to the selection of process conditions.

Measuring the film composition and crystallization kinetics during evaporation is nontrivial, requiring custom tools or access to synchrotron light sources.<sup>9,18</sup> Currently, the most accessible approaches couple *in situ* film-thickness measurements with evaporation models to predict the solvent composition and concentration over time.<sup>19–21</sup> However, these methods have only



been validated in carefully controlled laminar flow channels, often using solvent coatings without solute or single-solvent perovskite inks. Techniques such as *in situ* ellipsometry or white-light interferometry can offer subnanometer resolution but are challenging to adapt for drying perovskite coatings. More specifically, these techniques are hindered by the processes of nucleation and growth, which lead to inhomogeneous refractive indexes in the drying film that compromise the measurement.<sup>22,23</sup> Confocal chromatic sensors do not rely on changes in refractive index and therefore do not suffer from the same drawbacks as interferometry and ellipsometry.<sup>24</sup> However, their use in characterizing complex drying films in the perovskite literature is limited.

In this work, we use both white-light interferometry and chromatic confocal sensors to validate an isothermal lumped-parameter drying model that was previously used for single-solvent drying.<sup>21</sup> The model is expanded to include multi-solvent drying effects without the use of complicated fitting parameters. The coupling of model and film height measurement allows for the prediction of film composition as a function of time. The model only requires a single experimentally determined parameter, the mass-transfer coefficient ( $\beta$ ), from dynamic film-height-versus-time data to capture the characteristic convective environment of the coating setup. The model is used to develop parametric process paths that characterize the state of the drying film over time, i.e., solvent composition and solute concentration. Each process path in the model is found to represent a unique evolution of states, meaning that paths do not cross and initial ink composition largely predetermines the states accessible during drying. Process sensitivity is then quantified by comparing predicted evaporation rates based on variations in coating environment parameters, such as temperature, pressure, and solvent atmosphere. The process paths are not necessarily predictive of final film properties but rather capture formation conditions. We suggest that minimizing variations to the dynamic progression of drying liquid films along a process path will result in more reproducible and transferable processes. Furthermore, plotting process paths to a two-dimensional (2D) process map (solvent ratio versus solvent concentration) provides a framework for rational experimental design toward the development of scalable, high-performance MHP photovoltaics.

## RESULTS AND DISCUSSION

### Mixed-solvent evaporation model

A mixed-solvent, isothermal, lumped-parameter evaporation model is used to relate the change in film height and composition over time with the experimental convective environment, process conditions, and initial film composition. The generalized governing equations are described in the [Note S1](#) and can be extended to any solvent blend with an arbitrary number of components. The evaporation model only requires that the vapor pressure and approximate molar volumes of each pure component are known at the desired experimental conditions. In this work, two solvents (DMF and DMSO) and a perovskite salt are used to form a three-component system, given by

$$\frac{\partial \phi_{\text{DMF}}}{\partial t} = \frac{\beta}{h(t)} \left[ (\phi_{\text{DMF}} - 1) \frac{\rho_{\text{DMF}}^{\text{vap}} \bar{V}_{\text{DMF}}}{RT} X_{\text{DMF}} + \frac{\rho_{\text{DMSO}}^{\text{vap}} \bar{V}_{\text{DMSO}}}{RT} X_{\text{DMSO}} \right], \quad (\text{Equation 1})$$

$$\frac{\partial \phi_{\text{DMSO}}}{\partial t} = \frac{\beta}{h(t)} \left[ (\phi_{\text{DMSO}} - 1) \frac{\rho_{\text{DMSO}}^{\text{vap}} \bar{V}_{\text{DMSO}}}{RT} X_{\text{DMSO}} + \frac{\rho_{\text{DMF}}^{\text{vap}} \bar{V}_{\text{DMF}}}{RT} X_{\text{DMF}} \right], \quad (\text{Equation 2})$$

$$\frac{\partial h}{\partial t} = -\beta \left( \frac{\rho_{\text{DMF}}^{\text{vap}} \bar{V}_{\text{DMF}}}{RT} X_{\text{DMF}} + \frac{\rho_{\text{DMSO}}^{\text{vap}} \bar{V}_{\text{DMSO}}}{RT} X_{\text{DMSO}} \right), \quad (\text{Equation 3})$$

where  $t$  is time,  $h$  is film height,  $R$  is the gas constant,  $T$  is temperature,  $\phi_i$  is the volume fraction,  $\rho_i^{\text{vap}}$  is vapor pressure,  $\bar{V}_i$  is molar volume, and  $x_i$  is the mole fraction of solvent  $i$  in the wet film. Note that the use of volume fraction simplifies the derivation and can conveniently represent both liquid solvent and dissolved solute species. The equations are only written in terms of the solvents such that the perovskite solute is given by  $\phi_{\text{solute}} = 1 - \sum \phi_i$ . Here, a film is considered fully dried when  $\phi_{\text{solute}} = 0.999$ . The mass-transfer coefficient,  $\beta$ , is an empirical parameter and must be measured experimentally, while all other parameters may be determined beforehand based on the known solvent properties, ink recipe (solvent ratios and concentration), and process parameters (coating thickness and temperature).<sup>25</sup>  $\beta$  has units of m/s and quantifies the rate of solvent evaporated as a function of the convective environment for a given geometry and air flow rate. Note that others have devised a similar model whereby the mass-transfer coefficient depends on the solvent properties.<sup>14</sup> However, we show in the [supplemental information](#) that in the dilute limit a single mass-transfer coefficient is justified (see [Note S1](#)).

[Equations 1, 2, and 3](#) are simplified with three important assumptions: (1) that the liquid film is well mixed; (2) that the film and drying environment are isothermal; and (3) that the liquid and vapor species are ideal, and therefore there is no change in volume upon mixing. Assumption (1) implies that the impact of drying-driven vertical concentration gradients in the film are negligible. This assumption is validated using the mass-transfer Biot number ( $Bi_m$ ), which compares the vertical drying timescale with the vertical diffusion timescale.<sup>25,26</sup> In this work  $Bi_m = 0.14 \ll 1$ , indicating that diffusion in the vertical direction is fast compared to drying and can be ignored (see [Note S2](#)). Assumption (2) is justified by taking into account the thinness ( $\leq 5 \mu\text{m}$ ) of coated perovskite films and the heat transfer from the preheated glass substrate (see [Note S3](#), [Figure S3](#), and [Table S1](#)). The effect of the enthalpy of vaporization on film temperature for a 5- $\mu\text{m}$  solvent film on a glass slide held at 40°C is negligible. Note that the enthalpy of vaporization could have an effect if there is poor contact between the glass substrate and the heat source. Finally, assumption (3) is supported by the similar polarity of the two solvents under consideration in this study. However, this assumption is not always valid. Even in

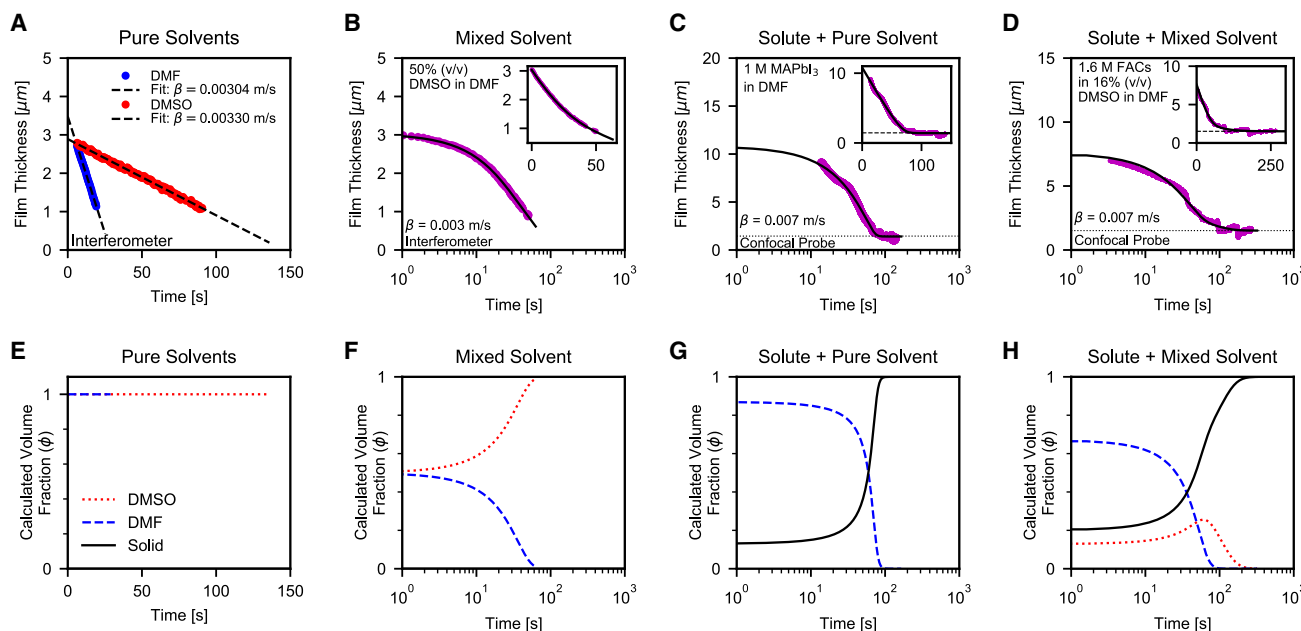


**Figure 1. Experimental *in situ* film-thickness measurements and comparison with evaporation-rate modeling**

(A) Pure DMF and DMSO measured via interferometry with  $\beta$  determined by linear fit.  
 (B) 50:50 (v/v) DMF/DMSO mixed solvent drying film measured via interferometry (points).  
 (C) 1 M MAPbI<sub>3</sub> in DMF measured via confocal probe (points).  
 (D) 1.6 M FA<sub>0.83</sub>CS<sub>0.17</sub>PbI<sub>3</sub> in 84:16 (v/v) DMF/DMSO measured via confocal probe (points). For (B)–(D), solid lines represent model predictions, where  $\beta$  was measured prior to coating using only pure solvents. Insets display results on time-linear coordinates.  
 (E–H) Model predicted component volume fractions corresponding to (A)–(D), respectively. Schematic and images describing the experimental setup are provided in Figures S4 and S5.

the case of nonideality, it is important to note that the trends and conclusions of this work would be unchanged. While additional complexity could be introduced into these models to more closely match specific coating conditions, the current assumptions are shown to be sufficient to understand the dynamics of evaporating perovskite films, and we believe the simplicity of these models offers the greatest utility to the coating and photovoltaics communities.

### Model validation via *in situ* film-thickness measurements

*In situ* film-thickness measurements are required to parameterize and validate the lumped-parameter evaporation model. First, simple drying-rate measurements with pure solvent films are used to determine  $\beta$ , which is found to sufficiently parameterize the evaporation model. In Figure 1A, the change in film height over time was measured via white-light interferometry. The experimentally measured film heights are shown as points, while a dashed line shows the linear fit used to determine  $\beta$ . After accounting for the difference in vapor pressure between DMF ( $p_{\text{DMF}}^{\text{vap}} = 1.34$  kPa) and DMSO ( $p_{\text{DMSO}}^{\text{vap}} = 0.22$  kPa) at a coating temperature of 40°C, both solvents show  $\beta = 0.003$  m/s. Additional measurements for  $\beta$  with pure DMF and DMSO are given in Figure S6. An average  $\beta \approx 0.003 \pm 0.0006$  m/s was obtained across 30°C–60°C.

A confocal probe was used to measure the change in film height for solute-containing coatings to avoid issues with

changes in optical properties with time. Unlike interferometry, the confocal probe measures the change in distance from the probe to the surface of the evaporating film (i.e., the air gap), which does not depend on the film's refractive index and is therefore a more robust and simpler measurement for systems with precipitation or crystallization. Due to the differences in the experimental setup, the mass-transfer coefficient for confocal measurements was different than that of interferometry,  $\beta = 0.007 \pm 0.003$  m/s for pure DMSO, indicating a higher air flow. It is important to note that all evaporation measurements were conducted in a nitrogen-atmosphere glovebox with a three-sided enclosure around the coating stage and all sources of convection (fans and purge valves) turned off. Thus, the evaporative environment is more controlled than typical coating stages, but the measured mass-transfer coefficient may vary significantly under less-controlled evaporative environments. When measured under identical environments,  $\beta$  values measured via interferometer and confocal probe were comparable, with a relative standard deviation of 17% of the mean (Table S2).

The lumped-parameter evaporation model requires inputs for the initial film height, material composition, and the experimentally determined value of  $\beta$ . Model predictions were validated against multi-component drying experiments. Three representative compositions were tested and are shown in Figures 1B–1D: a mixed solvent (DMF/DMSO), methylammonium lead iodide (MAPbI<sub>3</sub>) perovskite salt in single solvent (DMF), and a

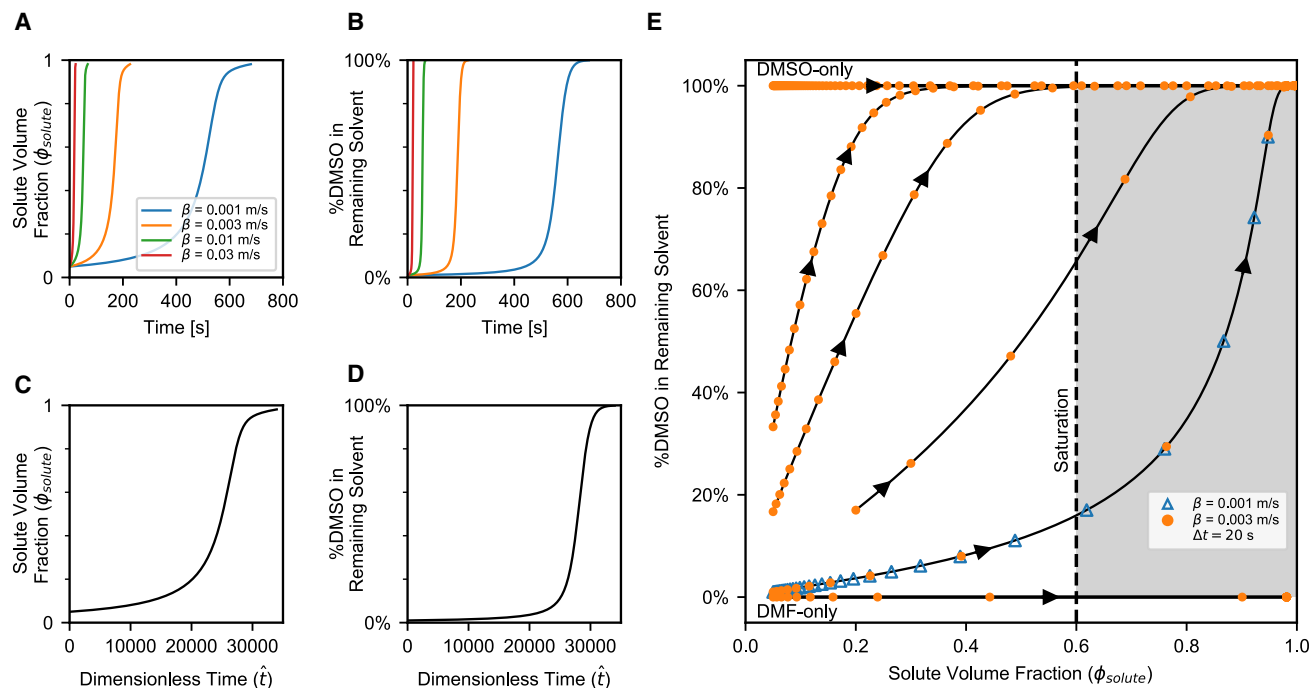


**Figure 2. Film composition and process paths calculated by the evaporation model**

(A–D) (A) Solute volume fraction and (B) %DMSO in remaining solvent versus time of an evaporating film at various  $\beta$ . (C) and (D) show that results in (A) and (B) collapse to a single curve over dimensionless time ( $\hat{t} = t/\tau_c$ , with characteristic timescale  $\tau_c = h_0/\beta$ , see Note S1), respectively.

(E) Process map with paths showing change in %DMSO and  $\phi_{\text{solute}}$  during drying. Time is implicit, and arrows indicate progression of time along process path. All points are spaced at 20-s intervals, and each film starts at  $\phi_{\text{solute}} = 0.05$ ,  $h_0 = 20$   $\mu\text{m}$ , and  $T = 40^\circ\text{C}$  except for one curve, which starts at  $\phi_{\text{solute}} = 0.2$  and  $h_0 = 5$   $\mu\text{m}$ .

formamidinium-cesium lead iodide ( $\text{FA}_{0.83}\text{Cs}_{0.17}\text{PbI}_3$ ) perovskite salt in a mixed solvent (DMF/DMSO). The  $\text{FA}_{0.83}\text{Cs}_{0.17}\text{PbI}_3$  in DMF/DMSO ink shown in Figure 1D is the same composition used to make the control devices shown in Figure 4. Figure 1B shows excellent agreement between model predictions (solid lines) and experimental data collected via interferometry. The time axes are displayed logarithmically to highlight the model accuracy at short times. Figure 1B shows two distinct evaporation regimes: the initial, faster-evaporation regime is predominately governed by DMF, while the later regime is dictated by the evaporation of DMSO. This is displayed explicitly in Figures 1F and 1H, which show that the relative volume fraction of DMSO increases as the film dries. Figure 1D demonstrates that the same co-solvent evaporation physics governs the evaporation rates of solute-containing inks. Note that the film height does not go to zero but approaches an average dry film thickness.<sup>21</sup> The minor discrepancies between model and data observed at early times is most likely due to disruptions in the film height during movement of the film from the coating station to the confocal probe station.

### Process paths describe unique evaporation process trajectories

A process path with its specific evolution within the process map of a liquid film can be constructed to capture the dynamic states of a drying film. The validated evaporation model is used to predict the rate of progression along the process path. First,

Figures 2A and 2B describe the change in  $\phi_{\text{solute}}$  and %DMSO in the solvent fraction as a function of time for various  $\beta$ . Slower convective evaporation rates (lower  $\beta$ ) take longer to dry, but the shape of the curve is fixed by the initial composition of the film. This is illustrated by Figures 2C and 2D, which collapse the curves in Figures 2A and 2B when time is scaled by  $h_0/\beta$ , respectively. Thus, a process path is constructed by plotting solvent fraction versus solute fraction, as shown in Figure 2E, such that time is implicit. While this study focuses on DMF/DMSO-based devices, common mixed-solvent systems like those with *N*-methylpyrrolidone (NMP) and dimethylacetamide (DMAc) can also be modeled as long as the solvent vapor pressures are known. To demonstrate the universal applicability of this methodology, Figure 2 was recreated for DMF/NMP and DMAc/DMSO mixtures in Figures S7 and S8. Detailed validation and experimental studies using these solvent systems are the subject of future work.

There are two important takeaways from the process-path map: (1) each process path is determined by the starting ink composition; and (2) process paths do not cross. Thus, the paths are unique, which also means that if a starting ink composition is created at a solvent ratio and solution concentration that overlaps with an existing process path, both films will ultimately follow the same path for the remainder of drying. Process parameters that affect convection, such as air flow rate and atmospheric pressure, only change the rate at which we move along a process path, not the trajectory. This is illustrated in Figure 2E

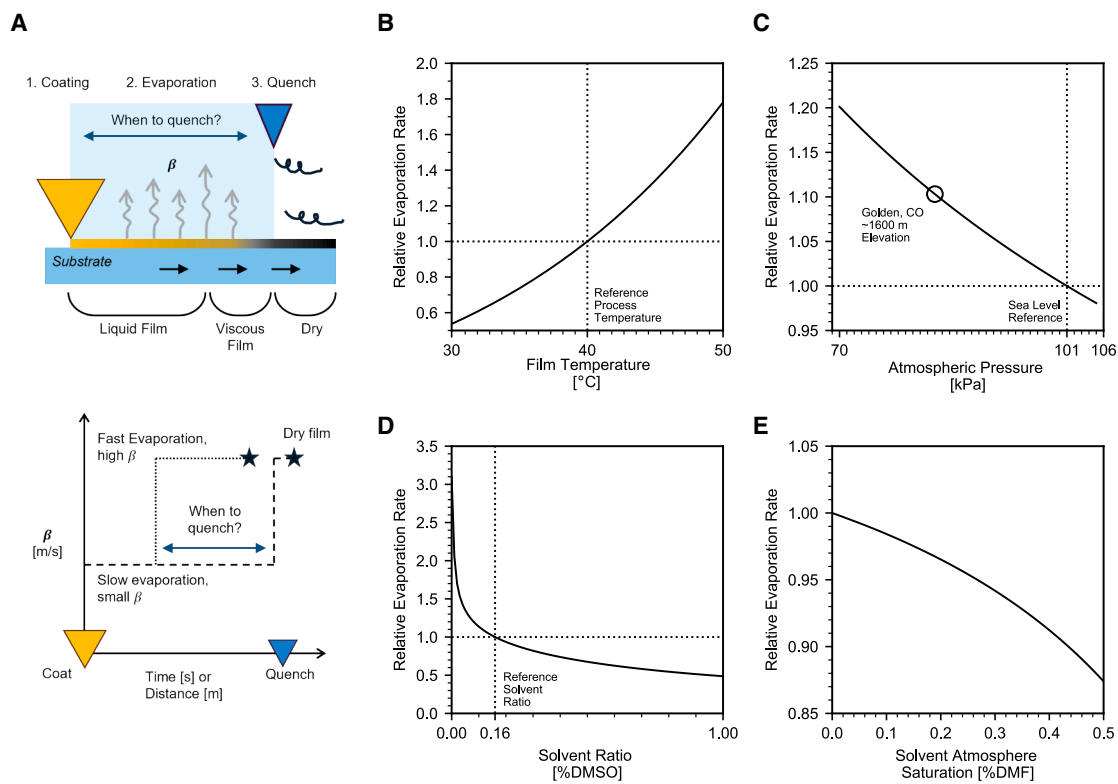


**Figure 3. Evaporation process sensitivity predicted by evaporation model**

(A) Schematic of general coating and drying process for perovskite thin films. Sensitivity of relative evaporation rate to (B) film temperature, (C) atmospheric pressure, (D) solvent ratio, and (E) solvent saturation of drying atmosphere. Dotted vertical and horizontal lines correspond to the same reference process condition.

using symbols to represent regularly spaced 20-s intervals for two different mass-transfer coefficients. The larger the mass-transfer coefficient, the faster the drying and larger the distance between 20-s intervals. The dashed line in Figure 2E represents the estimated saturation limit for a mixed-halide perovskite ( $\phi_{\text{solute}} \approx 0.6$ ) in a 4:1 mixture of DMF and DMSO, above which nucleation will occur.<sup>27</sup> In practice, the solubility boundary is a function of the solvent composition (%DMSO) in the film and must be determined under the relevant process conditions for each solute-solvent system. This is the subject of ongoing work but is outside the scope of the current study.

Process paths are relatively insensitive to processing conditions once an initial state has been established. For example, the process path is a very weak function of temperature. This arises because the relative vapor pressures of each solvent depend similarly on temperature. More specifically, for a 100°C change in temperature, the ratio of vapor pressures only change by a factor of 2 (Figure S9). Thus, the major effect of changing temperature is an increase in evaporation rate. Process paths are shown in Figure S9 for 20°C–100°C, representing a wide range of experimentally relevant temperatures. However, different temperatures could affect the final film morphology in ways not predicted by the model, due to changes in solubility and the kinetics of nucleation, ripening, and crystal growth.<sup>28–30</sup> Thus, conventional wisdom has correctly identified that engi-

neering of solvent ratio and concentration is the most effective way to move around the process map.<sup>31–33</sup>

Because evaporation rate does not change the process path, implementing a convective gas quench, as commonly discussed in the literature, does not change the process path.<sup>10–14</sup> Instead, a quench step, as shown in Figure 3A, would only be expected to accelerate the evolution of states of a drying film along a given path. However, if the process path crosses the saturation boundary during the quench, the accelerated drying could affect final film morphology. In other words, a quench step may only be expected to affect the final film morphology if the new evaporative conditions of the quench persist on or after the film has begun precipitation or nucleation. However, applying a quench step before precipitation or nucleation, as in most blade-coating studies, is only expected to decrease the time to saturation. This last point is tested in Figure 4.

A quantitative understanding of the solvent evaporation dynamics and the process-map framework offers valuable insight into early-stage process development. For example, spin coating SnPb MHP devices typically requires highly concentrated inks (>2 M) to achieve thicker absorber layers (1–2  $\mu\text{m}$ ). However, spin coating highly concentrated inks is challenging, as both the coating and quench processes must be executed with greater precision due to the rapid crystallization of the film. Recently, Abdollahi Nejad et al. demonstrated a

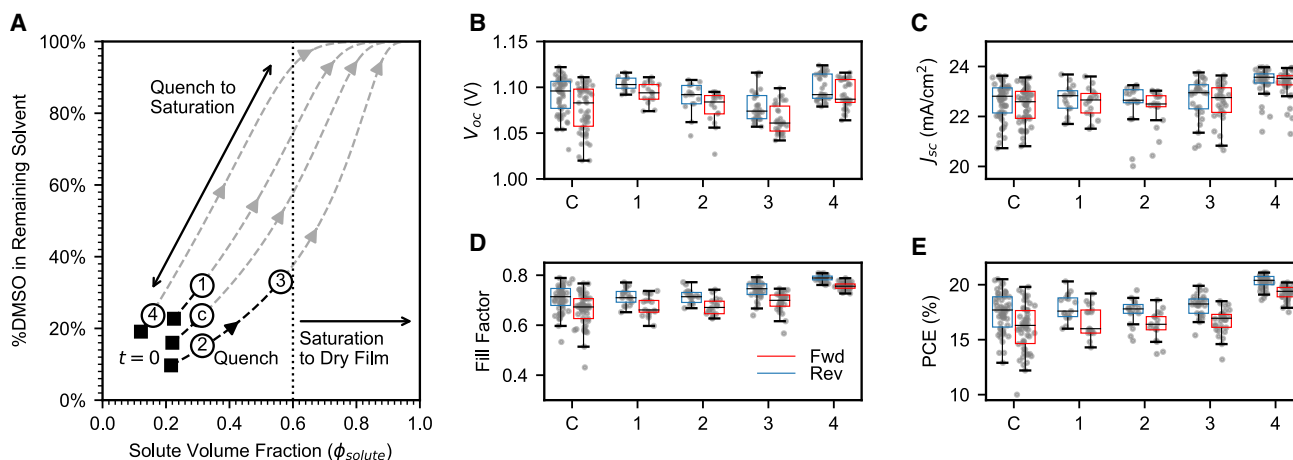


**Figure 4. Experimental process paths and corresponding device performance**

(A) Process-map design space indicating initial ink composition (squares) and state of the film at gas quench (labeled circles). Median and quartile box-and-whisker plots for (B) open-circuit voltage ( $V_{oc}$ ), (C) short-circuit current density ( $J_{sc}$ ), (D) fill factor, and (E) power-conversion efficiency (PCE) of photovoltaic devices made corresponding to process paths in (A). The box-and-whisker plots show the forward (red) and reverse (blue) scan data for each device. Representative current-voltage characteristics for champion devices are provided in Figure S11.

blade-coated tandem module using a 40% diluted ink based on their champion spin-coated device recipe (9:1 [v/v] DMF/DMSO).<sup>34</sup> The process-map framework reveals that without adjusting the DMF/DMSO ratio in the starting ink, the diluted ink follows a different process path during drying. This difference in solvent composition may, in part, help to explain the observed differences between their spin-coating devices and blade-coating devices. The process-map framework also shows that by carefully tuning the concentration and solvent ratios in the starting ink, it is possible to identify a set of dilute ink formulations that follow the same process path. This work suggests that scalable solution-processing techniques, such as blade coating, may offer better control over thicker coatings and more consistent crystallization, making them more suitable for the early research and development of SnPb devices compared to spin coating.

### Sensitivity of process dynamics

The rate at which a drying film moves along a process path depends only on  $\beta$ ,  $T$ ,  $p_{vap}$ , and  $h$ . Figures 3B–3E show predicted evaporation rates relative to a 5- $\mu$ m film coated with an initial ink composition of 20% solid volume fraction, 84%:16% DMF/DMSO, coated at 40°C, 101 kPa (1 atm), and  $\beta = 0.003$  m/s in a solvent-free (0% DMF) atmosphere. The same plots in total drying time (s) are given in Figure S10). As expected, evaporation rate depended most strongly on the drying temperature. Figure 3B shows the percent change in evaporation rate. For every 1°C away from 40°C, there is a roughly 5% shift in evaporation rate. Figure 3C shows that transferring processes between sites of different elevation could significantly affect the evaporation rate. Notably, moving from a facility at sea level (0 m) to the National Renewable Energy Laboratory (NREL) in Golden, Colorado (~1,600 m elevation) changes the evaporation rate by more than ~10%. Finally, Figures 3D and 3E illustrate how the solvent content in the coated film and drying air can significantly influ-

ence the evaporation rate. At low %DMSO, the evaporation rates become increasingly sensitive to the initial solvent formulation in the liquid phase. For the vapor phase, Equation 3 was derived, assuming that the bulk drying air is solvent free, i.e.,  $y_{bulk} = 0$ . However, enclosed evaporation environments or long-running continuous processes can create a concentrated solvent atmosphere around the evaporating film, suppressing the evaporation rate. While controlling the local solvent environment is challenging in practice, this offers a potential strategy to widen process windows and is the subject of ongoing work.

An important source of process sensitivity not discussed here is the variability in coating-film thickness, which would proportionally affect process timing. In slot-die coating, controlling the film thickness depends on the level of control over web speed, gap height, substrate thickness, and ink-dispense rate.<sup>35</sup> For example, a 1- $\mu$ m decrease in the coating thickness would reduce the total drying time by 20%, which is roughly equivalent to a 4°C shift in film temperature or 10% difference in the initial %DMSO content. The total drying time as a function of film height is also provided in Figure S10). Relative changes in evaporation rate provide a way to systematically compare process variables that have fundamentally different units of measurement. Understanding the evaporation rates within the context of the process maps highlights the impact that environmental process conditions can have on the reproducibility and transferability of scalable thin-film solution processing.

### Process-map framework uncovers process-performance relationships

The process map offers a rational basis for designing experiments to determine the effect of different parameters on final film morphology and device performance. Note that the evaporation model is solely based on the solvent evaporation dynamics and does not directly predict ideal processing conditions, morphology, or optoelectronic properties. Rather, the

model captures the evaporative environment and drying process, which we suggest is critical to process reproducibility and transferability. Determining the optimal process parameters for high-quality films still requires device fabrication. Therefore, the model and the process map provide a framework to set up process development experiments in which process-structure-performance relationships can be correlated. Moreover, this methodology provides an informed 2D design space and method of testing hypotheses rather than just variable optimization through a more costly blind multi-factor experimental design. For example, Figure 4 shows the drying process map for a formamidinium (FA) and cesium (Cs) mixed halide perovskite in a DMSO/DMF mixture. Five conditions were tested experimentally on four different process paths to investigate the effect of solvent composition, solute concentration, and quench timing (hold time between the film deposition and the start of the quench) on the performance of blade-coated devices. The evaporation model was used to calculate the required starting solvent composition and solute concentrations (Figure 4A, filled squares) of each ink to achieve a desired process condition at quench (Figure 4A, labeled open circles). Each experimental condition consisted of at least six substrates with eight devices per substrate. Conditions 1, 2, and C (control) have the same gas quench timing (14 s) and solute concentration at quench, but different amounts of %DMSO at quench as indicated by the open circles in Figure 4A. Conditions 2 and 3 share the same initial ink composition and, thus, process path, but have different quench times before saturation of 14 s and 35 s, respectively. Finally, conditions 4 and C have the same quench timing (14 s) and %DMSO at quench, but different solute concentrations.

Conditions 1, 2, and C are interesting test cases because they probe the effect of process path on the final device performance. One might expect that the three cases would result in different device performance because nucleation and growth are occurring under different solvent conditions. However, Figure 4E shows that, for this process, the %DMSO at quench or saturation does not significantly affect the median device PCE. Conditions 2 and 3 test the importance of quench time on final device performance. For example, Wang et al. found that applying a quench step after different hold times during spin coating resulted in different crystalline films with varying power-conversion efficiency (PCE).<sup>17</sup> However, Figure 4E shows that for these blade-coated films there is no statistically significant difference in the median PCE for two very different quench times, 14 s versus 35 s, respectively. The drying model provides one possible explanation for similar device performance of conditions C, 1, 2, and 3, which is that they all take a similar amount of time to dry after the quench (~13–20 s, see Table S3) and thus have similar film-formation dynamics. Since nucleation and growth are kinetic processes, the morphology of the final film is likely to be affected by the evaporation dynamics after saturation. Our previous work linked solid domain morphology to evaporation and crystallization dynamics in single-solvent inks, showing that evaporation rates mainly determine morphology, with faster evaporation leading to more uniform films and greater substrate coverage.<sup>36,37</sup> Drying times were calculated using the evaporation model assuming that

$\beta = 0.003$  m/s before quench and  $\beta = 0.03$  m/s during quench. An order-of-magnitude increase in  $\beta$  is a reasonable approximation for a gas quench, and the relative comparisons will not change for different values, since the same gas-quench procedure was used for each process.<sup>14</sup> These data suggest that the overall drying rate is an important correlation to final PCEs in blade-coated films, although more work is needed to test this hypothesis. It is clear that established processing steps critical in spin coating, such as quench timing, do not directly apply to all blade-coating processes.

Condition 4 is the only case that shows a significantly higher device performance (median PCE) and less variability (interquartile range) relative to all other process paths (see Tables S4–S6). The reproducibility of condition 4 was further confirmed by the final dry film thickness. Condition 4 exhibited the smallest standard deviation in device film thickness as measured by 3D laser scanning microscopy (Figure S12), suggesting a more reproducible coating and drying process. The process map and evaporation model also reveal two major differences for condition 4 that would not be discernible otherwise: nucleation and growth are occurring in the largest percentage of DMSO than in any other case, and condition 4 has the longest time between quench and drying (24.8 s). This suggests that perhaps a slower progression along a process path results in a more reproducible process that is less sensitive to quench timing, and that either there is a critical percentage of DMSO at saturation that leads to better device performance or that the time from quench to dried film is an important parameter. Additional experiments are planned to test these hypotheses for more process paths and longer drying times and to test whether similar relationships hold in other ink systems such as DMF/NMP and DMAc/DMSO. While the scope of this study was focused on device PCE, a similar evaluation methodology can be used for process-structure relationships such as morphology or optoelectronic properties (e.g., pinholes, grain size, defect states, device performance, and density of states). On a process map, characterization is only comparable under identical experimental conditions. For example, understanding the effect of the coating substrate on final film morphology would require constructing separate process maps for each substrate. Establishing ideal process conditions then involves experimental development across each process map to quantify how the substrate growth surface affects morphology in the context of the process drying dynamics. Taken together, these data demonstrate a new strategy toward scalable perovskite development. By applying process sensitivity analysis and evaporation-rate modeling, we better understand how variations in a localized environment can affect a process and enable the development of a less-sensitive process path. The process development methodology of quantifying the evaporative environment ( $\beta$ ), modeling evaporation process paths, and accounting for environmental changes ultimately provides a framework for reducing variability and enabling process transfer between variable environments (e.g., laboratories or institutions).

This study develops an approach based on a simple lumped-parameter evaporation model to quantify the drying behavior in perovskite thin films. The model allows the characteristic convective environment to be captured by a single parameter,

the mass-transfer coefficient ( $\beta$ ). This coefficient  $\beta$  was measured from evaporation of pure solvent coatings and was found to be sufficient to predict the change in film height over time for more complicated solute-solvent and mixed-solvent systems. The equations presented are easily adapted to predict drying of thin films with an arbitrary number of volatile and nonvolatile components. Using two *in situ* techniques (white-light interferometry and chromatic confocal distance measurements), the variability in  $\beta$  was found to be <20%.

A process map was constructed, capturing every possible compositional state of a solution. The evaporation model was used to draw process paths, describing the unique progression of states (solvent composition and concentration) over time for a mixed-solvent perovskite ink. Process paths were found to depend on the initial formulation of the film, and once established they were surprisingly difficult to shift. The model predicted that variables such as temperature only had a limited effect on the position of the process path, even over a temperature range of 80°C. However, the rate that a specific process progressed along its path was proportional to the evaporation rate. The model also indicates that the temperature of the drying film and  $\beta$  likely have the greatest influence on the variability of the evaporation rate. The variability in these dynamics as a function of the process environment (e.g., convection, temperature, and atmospheric pressure) were hypothesized to lead to variability in final device performance. In other words, the robustness of a process depends on how much its state changes with variability in process evaporation rate.

Insights from the process-path methodology were applied to the development of scalable perovskite processing by engineering ink systems to decouple the effect of solvent ratio and solute concentration at the point of film quenching. Of the conditions tested, it was found that neither the %DMSO at quench nor quench timing significantly impacted the final device efficiency but that ink dilution was found to improve the median PCE and significantly reduce variability compared to the established control condition. The evaporation model and process maps were able to identify two important process differences between the dilute condition compared to the other process paths tested: that nucleation and growth likely occurred in the highest %DMSO and that it took the longest time to completely dry after quench. These results suggest that existing recipes could also be further improved within this framework. Using the process paths developed in this work to couple the effects of ink engineering, localized process environment, and processing sensitivity will enable the development of more reproducible and transferable deposition methods for scalable MHP technologies.

## METHODS

### Materials preparation

The substrates used were 50 × 50-mm patterned indium-doped tin-oxide-coated soda lime glass (<20 Ω/sq) obtained from Colorado Concept Coatings (CCC). Cesium iodide (CsI, 99.999%), ethanol (EtOH, 95%), aluminum oxide nanoparticles, and DMF (anhydrous, 99.8%) were purchased from Sigma-Aldrich. Lead (II) iodide (PbI<sub>2</sub>, 99.99%), [2-(3,6-dimethyl-9H-carbazol-9-yl)ethyl]phosphonic acid (Me-4PACz, >99.0%), and bathocuproine

(BCP, purified by sublimation) were purchased from TCI Chemicals. Carbon-60 (C60, <99.5%) was purchased from Luminescence Technology. Formamidinium iodide was purchased from Greatcell Solar Materials. The nickel oxide target (NiOx, 99.9%) and silver pellets (Ag, 99.9%) were purchased from the Kurt J. Lesker Company.

### Thin film and device fabrication

Devices were made on glass substrates coated with indium-doped tin oxide. Substrates were first cleaned in a Liquinox detergent and water solution, sonicated for 10 min each in deionized water, acetone, and isopropyl alcohol, and blown dry with nitrogen in between each step. The substrates were then cleaned in a Jel-light Company, Inc. Model 30 UV/ozone using ambient air for 15 min, then immediately transferred into a Denton Explorer sputter chamber for nickel oxide deposition. The sputter target is conditioned for 1,000 s followed by a 400-s deposition step, resulting in a nickel oxide thickness of 5 nm. Before use, the nickel oxide layer was annealed for 10 min at 300°C in ambient air with relative humidity at approximately 20%–40%. All subsequent deposition steps were performed in a nitrogen environment. A 0.5 mg/mL solution of Me-4PACz was spin coated on top of the nickel oxide layer at 3,000 rpm for 30 s and annealed for 10 min at 100°C. Thereafter, a 0.5 wt % aluminum oxide nanoparticle solution was deposited on a Specialty Coating System GP3 spin coater at 6,000 rpm for 30 s to improve surface wetting. The substrates were then transferred to a Zehntner ZAA 2300 blade coater for deposition of the perovskite active layer.

The active layer was deposited via blade coating with a nitrogen quench from an air knife following the blade. The blade coater platen was heated to 40°C prior to coating, which was chosen based on a prior temperature-device optimization study using the same formulation. The ink was deposited at 7.5 mm/s. The air knife was set 0.5 inches (0.27 cm) above and perpendicular to the substrate and passed over at 7.5 mm/s with a nitrogen flow rate of 6.8 SCFM. The quench timings used for each film are reported in Table S3, and corresponding perovskite ink compositions and coating conditions for each device are summarized in Table S7. The gap height of the blade was set to 50 μm for the control and conditions 1–3 and used 20 μL of solution deposited between the blade and substrate. For device condition 4, the gap height was set to 75 μm and used 80 μL of perovskite ink. Changing these parameters ensured a final dry film of approximately the same thickness across each condition. A Keyence VK-X250 series 3D laser scanning microscope was used to measure dry film thicknesses after coating. Each film was scribed to identify the substrate surface for an absolute measurement of the perovskite film thickness. Once the active layer was deposited, the electron-transport layer and the contacts were thermally evaporated in an Angstrom evaporator.

### Characterization and measurements

J-V scans were measured in an inert nitrogen glovebox with a Keithley 2450 source-measure unit. Sweeps were taken from –0.2 V to 1.2 V at a rate of 0.8 V/s. Illumination was provided by a class AAA LED G2V solar simulator calibrated with an AM 1.5G filter. A calibrated silicon reference cell is used to ensure the light source is set to the correct intensity before

measurements. Spectrum data were measured for both the lamp and the calibrated diode, from which a mismatch factor was calculated. The lamp is calibrated approximately every 6 months and the reference cell approximately every year. Each substrate was divided into eight devices with an area of 0.228 cm<sup>2</sup> per device. When testing each device, a metal mask is added for an illuminated active area of 0.14 cm<sup>2</sup>. Light soaking and maximum power-point tracking were used to ensure each device reached steady-state performance before recording the device scans. All devices were tested at room temperature in a nitrogen glovebox, keeping the oxygen and humidity at 0 ppm during testing. There was a small fan placed near the sample stage to keep air flow over the sample and to reduce heating effects of the lamp during measurements. Devices that were shunted or otherwise affected/nonfunctional were dropped prior to compiling device statistics.

### **In situ film-thickness measurements**

Evaporation rate was measured by either white-light interferometry or confocal displacement. Confocal measurements were made using a Micro-epsilon IFS2405-01 confocal displacement sensor to measure the absolute displacement of the top surface of the drying film. A high-resolution probe was required for thin films below 10 μm. The drying curves in Figures 1C and 1D had an offset of 1 μm applied to the lowest data point to approximate the average dry film thicknesses (not shown). Using a second probe *in situ* to track the position of the bare substrate would allow the confocal probe to produce absolute film-thickness measurements. Confocal measurements shown in Figures 1B–1D were measured at 30°C to avoid condensation on the confocal probe tip at the required working distance of 100 μm. The close working distance did not appear to affect the convective environment around the film, and strategies such as heating of the probe can be employed to avoid condensation. Since the precise time between coating and the start of data collection is unknown in the current setup, a time-shift procedure was applied to estimate the delay (Figures S13 and S14). A labeled diagram of the experimental setup is provided in Figure S5. Interferometry thickness measurements were made using an Ocean Insight HR4Pro white-light interferometer with a collimating lens. Further details regarding the interferometer peak fitting procedure are provided in Figures S15 and S16.

### **Modeling**

All modeling and data processing were performed in Python. A list of solvent parameters is also provided for other common ink solvents in Table S8.

### **RESOURCE AVAILABILITY**

#### **Lead contact**

Requests for further information and resources should be directed to and will be fulfilled by the lead contact, Axel Palmstrom ([axel.palmstrom@nrel.gov](mailto:axel.palmstrom@nrel.gov)).

#### **Materials availability**

This study did not generate new materials.

#### **Data and code availability**

- All other data reported in this paper will be shared by the lead contact upon request.

- All original code has been deposited at Zenodo (<https://doi.org/10.5281/zenodo.15282351>)<sup>38</sup> and is publicly available as of the date of publication.
- Any additional information required to reanalyze the data reported in this paper is available from the lead contact upon request.

### **ACKNOWLEDGMENTS**

Efforts by J.L.S., N.J.A., and R.A.C. were supported by the National Science Foundation grant CMMI-933819, and J.L.S. also received support for work at NREL from the US Department of Energy (DOE) Office of Science and Graduate Student Research Program (SCGSR). The work by A.E.L., R.A.K., E.A.G., R.W.E., R.C.B., J.J.B., K.Z., and A.F.P. was supported by the National Renewable Energy Laboratory for the US DOE under contract no. DE-AC36-08GQ28308. Funding was provided by the US DOE Office of Energy Efficiency and Renewable Energy Solar Technologies Office under awards #38256 and #52776. The views expressed in the article do not necessarily represent the views of the DOE or the US Government. The US Government retains and the publisher, by accepting the article for publication, acknowledges that the US Government retains a nonexclusive, paid-up, irrevocable, worldwide license to publish or reproduce the published form of this work, or allow others to do so, for US Government purposes.

### **AUTHOR CONTRIBUTIONS**

Conceptualization, J.L.S., A.F.P., N.J.A., and R.A.C.; methodology, J.L.S., A.E.L., R.W.E., and E.A.G.; investigation, J.L.S. and A.E.L.; writing – original draft, J.L.S. and A.E.L.; writing – review & editing, K.S., E.A.G., R.W.E., R.C.B., R.A.K., K.Z., J.J.B., R.A.C., N.J.A., and A.F.P.; funding acquisition, J.L.S., A.F.P., J.J.B., N.J.A., and R.A.C.; resources, A.F.P.; supervision, A.F.P., N.J.A., and R.A.C.

### **DECLARATION OF INTERESTS**

The authors declare no competing interests.

### **SUPPLEMENTAL INFORMATION**

Supplemental information can be found online at <https://doi.org/10.1016/j.xcrp.2025.102655>.

Received: January 10, 2025

Revised: March 24, 2025

Accepted: May 21, 2025

Published: June 18, 2025

### **REFERENCES**

1. National Renewable Energy Laboratory} (2024). Best research-cell efficiency chart. . URL: <https://www.nrel.gov/pv/cell-efficiency.html>.
2. National Renewable Energy Laboratory} (2024). Champion photovoltaic module efficiency chart. . URL: <https://www.nrel.gov/pv/module-efficiency.html>.
3. Dunlap-Shohl, W.A., Zhou, Y., Padture, N.P., and Mitzi, D.B. (2019). Synthetic Approaches for Halide Perovskite Thin Films. *Chem. Rev.* 119, 3193–3295. <https://doi.org/10.1021/acs.chemrev.8b00318>.
4. Jeon, N.J., Noh, J.H., Kim, Y.C., Yang, W.S., Ryu, S., and Seok, S.I. (2014). Solvent engineering for high-performance inorganic–organic hybrid perovskite solar cells. *Nat. Mater.* 13, 897–903. <https://doi.org/10.1038/nmat4014>.
5. Kim, H.B., Choi, H., Jeong, J., Kim, S., Walker, B., Song, S., and Kim, J.Y. (2014). Mixed solvents for the optimization of morphology in solution-processed, inverted-type perovskite/fullerene hybrid solar cells. *Nanoscale* 6, 6679–6683. <https://doi.org/10.1039/c4nr00130c>.

6. Salim, T., Sun, S., Abe, Y., Krishna, A., Grimsdale, A.C., and Lam, Y.M. (2015). Perovskite-based solar cells: impact of morphology and device architecture on device performance. *J. Mater. Chem. A Mater.* **3**, 8943–8969. <https://doi.org/10.1039/C4TA05226A>.
7. Yang, M., Li, Z., Reese, M.O., Reid, O.G., Kim, D.H., Siol, S., Klein, T.R., Yan, Y., Berry, J.J., van Hest, M.F.A.M., and Zhu, K. (2017). Perovskite ink with wide processing window for scalable high-efficiency solar cells. *Nat. Energy* **2**, 17038. <https://doi.org/10.1038/nenergy.2017.38>.
8. Zhang, L., Li, B., Yuan, J., Wang, M., Shen, T., Huang, F., Wen, W., Cao, G., and Tian, J. (2018). High-Voltage-Efficiency Inorganic Perovskite Solar Cells in a Wide Solution-Processing Window. *J. Phys. Chem. Lett.* **9**, 3646–3653. <https://doi.org/10.1021/acs.jpcllett.8b01553>.
9. Shargaieva, O., Näsström, H., Smith, J.A., Többsens, D., Munir, R., and Unger, E. (2020). Hybrid perovskite crystallization from binary solvent mixtures: interplay of evaporation rate and binding strength of solvents. *Mater. Adv.* **1**, 3314–3321. <https://doi.org/10.1039/D0MA00815J>.
10. Sun, J., Li, F., Yuan, J., and Ma, W. (2021). Advances in Metal Halide Perovskite Film Preparation: The Role of Anti-Solvent Treatment. *Small Methods* **5**, 2100046. <https://doi.org/10.1002/smt.202100046>.
11. Gu, L., Fei, F., Xu, Y., Wang, S., Yuan, N., and Ding, J. (2022). Vacuum Quenching for Large-Area Perovskite Film Deposition. *ACS Appl. Mater. Interfaces* **14**, 2949–2957. <https://doi.org/10.1021/acsami.1c22128>.
12. Sánchez, S., Jerónimo-Rendon, J., Saliba, M., and Hagfeldt, A. (2020). Highly efficient and rapid manufactured perovskite solar cells via Flash InfraRed Annealing. *Mater. Today* **35**, 9–15. <https://doi.org/10.1016/j.mat-tod.2019.11.003>.
13. Yu, Y., Zhang, F., Hou, T., Sun, X., Yu, H., and Zhang, M. (2021). A Review on Gas-Quenching Technique for Efficient Perovskite Solar Cells. *Sol. RRL* **5**, 2100386. <https://doi.org/10.1002/solr.202100386>.
14. Ternes, S., Mohacsí, J., Lüdtkke, N., Pham, H.M., Arslan, M., Scharfer, P., Schabel, W., Richards, B.S., and Paetzold, U.W. (2022). Drying and Coating of Perovskite Thin Films: How to Control the Thin Film Morphology in Scalable Dynamic Coating Systems. *ACS Appl. Mater. Interfaces* **14**, 11300–11312. <https://doi.org/10.1021/acsami.1c22363>.
15. Kerner, R.A., Zhao, L., Xiao, Z., and Rand, B.P. (2016). Ultrasoft metal halide perovskite thin films via sol-gel processing. *J. Mater. Chem. A Mater.* **4**, 8308–8315. <https://doi.org/10.1039/C6TA03092K>.
16. Munir, R., Sheikh, A.D., Abdelsamie, M., Hu, H., Yu, L., Zhao, K., Kim, T., Tall, O.E., Li, R., Smilgies, D.M., and Amassian, A. (2017). Hybrid perovskite thin-film photovoltaics: in situ diagnostics and importance of the precursor solvate phases. *Adv. Mater.* **29**, 1604113. <https://doi.org/10.1002/adma.201604113>.
17. Wang, K., Tang, M.C., Dang, H.X., Munir, R., Barrit, D., De Bastiani, M., Aydin, E., Smilgies, D.M., De Wolf, S., and Amassian, A. (2019). Kinetic stabilization of the sol-gel state in perovskites enables facile processing of high-efficiency solar cells. *Adv. Mater.* **31**, 1808357. <https://doi.org/10.1002/adma.201808357>.
18. Ternes, S., Laufer, F., Scharfer, P., Schabel, W., Richards, B.S., Howard, I. A., and Paetzold, U.W. (2022). Correlative In Situ Multichannel Imaging for Large-Area Monitoring of Morphology Formation in Solution-Processed Perovskite Layers. *Sol. RRL* **6**, 2100353. <https://doi.org/10.1002/solr.202100353>.
19. Schmidt-Hansberg, B., Klein, M.F.G., Peters, K., Buss, F., Pfeifer, J., Walheim, S., Colmann, A., Lemmer, U., Scharfer, P., and Schabel, W. (2009). In situ monitoring the drying kinetics of knife coated polymer-fullerene films for organic solar cells. *J. Appl. Phys.* **106**, 124501. <https://doi.org/10.1063/1.3270402>.
20. Schmidt-Hansberg, B., Baunach, M., Krenn, J., Walheim, S., Lemmer, U., Scharfer, P., and Schabel, W. (2011). Spatially resolved drying kinetics of multi-component solution cast films for organic electronics. *Chem. Eng. Process. Process Intensif.* **50**, 509–515. <https://doi.org/10.1016/j.cep.2010.12.012>.
21. Ternes, S., Börnhorst, T., Schwenzer, J.A., Hossain, I.M., Abzieher, T., Mehlmann, W., Lemmer, U., Scharfer, P., Schabel, W., Richards, B.S., and Paetzold, U.W. (2019). Drying Dynamics of Solution-Processed Perovskite Thin-Film Photovoltaics: In Situ Characterization, Modeling, and Process Control. *Adv. Energy Mater.* **9**, 1901581. <https://doi.org/10.1002/aenm.201901581>.
22. K. Hinrichs and K.J. Eichhorn, eds. (2018). *Ellipsometry of Functional Organic Surfaces and Films*. Vol. 52 of Springer Series in Surface Sciences (Springer International Publishing). <https://doi.org/10.1007/978-3-319-75895-4>.
23. Harrick, N.J. (1971). Determination of Refractive Index and Film Thickness from Interference Fringes. *Appl. Opt.* **10**, 2344–2349. <https://doi.org/10.1364/AO.10.002344>.
24. Zhou, D.w., Gambaryan-Roisman, T., and Stephan, P. (2009). Measurement of water falling film thickness to flat plate using confocal chromatic sensing technique. *Exp. Therm. Fluid Sci.* **33**, 273–283. <https://doi.org/10.1016/j.expthermflusci.2008.09.003>.
25. Bird, R.B., Stewart, W.E., and Lightfoot, E.N. (2007). *Transport Phenomena, Revised ed.* (Wiley).
26. Cussler, E.L. (2009). *Diffusion: Mass Transfer in Fluid Systems, 3rd ed.* (Cambridge University Press) 978-0-521-87121-1.
27. Petrov, A.A., Ordinaisev, A.A., Fateev, S.A., Goodilin, E.A., and Tarasov, A.B. (2021). Solubility of Hybrid Halide Perovskites in DMF and DMSO. *Molecules (Basel)* **26**, 7541. <https://doi.org/10.3390/molecules26247541>.
28. Alexandrov, D.V., and Nizovtseva, I.G. (2014). Nucleation and particle growth with fluctuating rates at the intermediate stage of phase transitions in metastable systems. *Proc. R. Soc. A A.* **470**, 20130647. <https://doi.org/10.1098/rspa.2013.0647>.
29. Qiu, S., Majewski, M., Dong, L., Jang, D., Corre, V.M.L., Cerrillo, J.G., Ronsin, O.J.J., Yang, F., Guo, F., Zhang, K., et al. (2024). In Situ Probing the Crystallization Kinetics in Gas-Quenching-Assisted Coating of Perovskite Films. *Adv. Energy Mater.* **14**, 2303210. <https://doi.org/10.1002/aenm.202303210>.
30. Majewski, M., Qiu, S., Ronsin, O., Lüer, L., Corre, V.M.L., Du, T., Brabec, C.J., Egelhaaf, H.J., and Harting, J. (2025). Simulation of perovskite thin layer crystallization with varying evaporation rates. *Mater. Horiz.* **12**, 555–564. <https://doi.org/10.1039/d4mh00957f>.
31. Li, G., Wang, Z., Wang, Y., Yang, Z., Dong, P., Feng, Y., Jiang, Y., Feng, S. P., Zhou, G., Liu, J.M., and Gao, J. (2023). Co-Solvent Engineering Contributing to Achieve High-Performance Perovskite Solar Cells and Modules Based on Anti-Solvent Free Technology. *Small (Weinh.)* **19**, 2301323. <https://doi.org/10.1002/sml.202301323>.
32. Zhang, H., Darabi, K., Nia, N.Y., Krishna, A., Ahlawat, P., Guo, B., Almalki, M.H.S., Su, T.S., Ren, D., Bolnykh, V., et al. (2022). A universal co-solvent dilution strategy enables facile and cost-effective fabrication of perovskite photovoltaics. *Nat. Commun.* **13**, 89. <https://doi.org/10.1038/s41467-021-27740-4>.
33. Li, J., Dagar, J., Shargaieva, O., Flatken, M.A., Köbler, H., Fenske, M., Schultz, C., Stegemann, B., Just, J., Többsens, D.M., et al. (2021). 20.8% Slot-Die Coated MAPbI<sub>3</sub> Perovskite Solar Cells by Optimal DMSO-Content and Age of 2-ME Based Precursor Inks. *Adv. Energy Mater.* **11**, 2003460. <https://doi.org/10.1002/aenm.202003460>.
34. Abdollahi Nejad, B., Ritzer, D.B., Hu, H., Schackmar, F., Moghadamzadeh, S., Feeney, T., Singh, R., Laufer, F., Schmager, R., Azmi, R., et al. (2022). Scalable two-terminal all-perovskite tandem solar modules with a 19.1% efficiency. *Nat. Energy* **7**, 620–630. <https://doi.org/10.1038/s41560-022-01059-w>.

35. Carvalho, M.S., and Khashgi, H.S. (2000). Low-flow limit in slot coating: Theory and experiments. *AIChE J.* 46, 1907–1917. <https://doi.org/10.1002/aic.690461003>.
36. Starger, J.L., Fafarman, A.T., Baxter, J.B., Alvarez, N.J., and Cairncross, R.A. (2023). Quasi-2D Model to Predict Solid Microstructure in Drying Thin Films. *Langmuir* 39, 3c01469. <https://doi.org/10.1021/acs.langmuir.3c01469>.
37. Hossain, M., Starger, J.L., Efyrow, J.J., Barrett, R.F., Bolduc, J.S., Alvarez, N.J., Cairncross, R.A., Fafarman, A.T., and Baxter, J.B. (2024). Retrograde Solubility of Methylammonium Lead Iodide in  $\gamma$ -Butyrolactone Does Not Enhance the Uniformity of Continuously Coated Films. *Langmuir* 40, 8836–8842. <https://doi.org/10.1021/acs.langmuir.3c03979>.
38. jstarger (2025). jstarger/DryingCode: v1.0.0 (Zenodo). <https://doi.org/10.5281/zenodo.15282352>.